Electronic states in superconducting type-II Dirac semimetal: 1T-PdSeTe

Yogendra Kumar, ^{1,2,*} Shiv Kumar, ^{2,†} Venkateswara Yenugonda, ³ Ryohei Oishi, ¹ Jayita Nayak, ⁴ Chaoyu Chen, ⁵ Ravi Prakash Singh, ⁶ Takahiro Onimaru, ¹ Yasuyuki Shimura, ¹ Shinichiro Ideta, ^{1,2} and Kenya Shimada^{1,2,7,8,‡}

¹Graduate School of Advanced Science and Engineering,
Hiroshima University, Higashi-Hiroshima 7390046, Japan

²Research Institute for Synchrotron Radiation Science (HiSOR),
Hiroshima University, Higashi-Hiroshima 739-0046, Japan

³Department of Physics, SUNY Buffalo State University, New York 14222, U.S.A

⁴Department of Physics, Indian Institute of Technology, Kanpur 208016, India

⁵Shenzhen Institute for Quantum Science and Engineering (SIQSE) and Department of Physics,
Southern University of Science and Technology (SUSTech), Shenzhen 518055, China

⁶Department of Physics, Indian Institute of Science Education and Research, Bhopal 462066, India

⁷The International Institute for Sustainability with Knotted Chiral Meta Matter (WPI-SKCM²),
Hiroshima University, Higashi-Hiroshima 739-0046, Japan

⁸Research Institute for Semiconductor Engineering (RISE),
Hiroshima University, Higashi-Hiroshima 739-8527, Japan
(Dated: August 29, 2024)

We have investigated the surface and bulk electronic structures of the superconducting type-II Dirac semimetal 1T-PdSeTe. The superconducting transition temperature $T_C=3.2~\rm K$ was almost twice as high as $T_C=1.6~\rm K$ in 1T-PdTe₂. Scanning transmission electron microscopy measurements showed homogeneously mixed Se and Te atoms in the chalcogen layers, consistent with the CdI₂-type crystal structure. Angle-resolved photoemission spectroscopy measurements and density functional theory calculations indicated the existence of the topological surface states, and the overall band structures were similar to those of 1T-PdTe₂. These results suggest that CdI₂-type lattice symmetry dictates the band dispersion, regardless of atomic disorder in the chalcogen layers. As the electronic band dispersion and the local structures were persistent upon substitution, the enhancement of T_C is likely associated with the chemical pressure. Our results provide insight into the effects of the solid solution on the surface and bulk electronic states as well as the superconducting transition temperature.

I. INTRODUCTION

Topological semimetals have been the focus of recent theoretical and experimental studies 1,2 . Dirac semimetals, Weyl semimetals, and topological nodal-line semimetals are the three major categories characterized by the form and degeneracy of the band crossings as well as spin texture near the Fermi level $(E_{\rm F})^{3,4}$.

Weyl semimetals can be realized by breaking either the spatial inversion symmetry or the time-reversal symmetry of Dirac semimetals 5 . They are characterized by massless chiral fermions in the bulk behaving like magnetic monopoles in momentum space (i.e., Weyl fermions) and discontinuous Fermi arcs in the topological surface states. Weyl semimetals may exhibit high-charge-carrier mobility and high negative magnetoresistance under strong electric and magnetic fields, which was discussed in terms of the Adler-Bell-Jackiw anomaly (nonconservation of chiral current in the presence of gauge fields) in quantum field theory 6 .

There are two types of Weyl semimetals: type I with Lorentz symmetry such as TaAs, and type II without Lorentz symmetry such as WTe₂ and $\mathrm{MoTe_2}^4$. The anisotropic chiral anomaly in the type-II Weyl semimetals induces the anisotropic magneto-transport properties⁷.

In the search for type-II Weyl semimetals, $1T-PdTe_2$

has attracted much attention because it is a type-II Dirac semimetal and exhibits superconductivity⁸⁻¹⁰. Due to the centrosymmetric and nonsymmorphic properties of 1T-PdTe₂, some of the Kramers doublets degenerate at the zone boundary. Furthermore, 1T-PdTe₂ has several tilted Dirac points in the bulk along the Γ -A direction of the bulk Brillouin zone. These Dirac points are protected by the strong spin-orbit interaction because the symmetry of the $R_{5,6}^+$ states with J=3/2 (at the Γ point) derived from Te $5p_x$, $5p_y$ orbitals cannot hybridize with the R_4^- state with J=1/2 (at the Γ point) derived from Te $5p_z$ orbital due to different J values¹¹. In addition, 1T-PdTe₂ hosts several topological surface states (TSSs) in the gap of the bulk bands with inverted parity 10,11 . The TSS is robust under perturbations that conserve the topological numbers, exhibiting high carrier mobility, the quantum spin Hall effect¹², the quantum anomalous Hall effect¹³, Majorana fermions in the superconducting state¹⁴, and magnetic monopoles¹⁵.

As concerns superconducting property, 1T-PdTe₂ was reported to be a type-II superconductor with $T_C=1.64~\rm K^{8-10}$. The bulk superconductivity in 1T-PdTe₂ can be understood from the conventional BCS theory in which Cooper pairs are formed via the electron-phonon interaction^{9,13}. The density functional theory (DFT) calculations indicated significant role of a van Hove singularity derived from the saddle point near the M point in the bulk superconductivity^{16,17}. On the other hand, surface

superconductivity has been identified^{5,6,8,12,18,19} and the ac-susceptibility measurement showed an unusual surface sheath superconductivity, which is likely related to the TSS in 1T-PdTe₂^{12,20}. Note that non-trivial Berry phase has been reported in the de Haas-van Alphen quantum oscillation measurements^{21,22}.

To realize the Weyl semimetal starting from 1T-PdTe₂, one can break time-reversal symmetry by introducing magnetic elements or break the inversion symmetry by modifying the lattice²³. In the case of 1T-PdTe₂, it has been suggested to completely substitute one of the Te layers in 1T-PdTe₂ with the Se layer to eliminate inversion symmetry point, and, indeed, the density functional theory (DFT) calculations indicated lifting of band degeneracy near the zone boundary¹¹.

Recently, the superconducting transition temperature of 1T-PdSeTe was reported to be $T_C=2.74~\mathrm{K}^{8,24}$, which was 1.67 times larger than that of 1T-PdTe₂ ($T_C=1.64~\mathrm{K}$)⁸. The magnetic susceptibility and heat capacity measurements showed the type-II superconductivity with large anisotropy and non-bulk superconductivity with a volume fraction of 20%⁸. The reason for the enhanced T_C was discussed based on chemical pressure effect and defects/disorder effect⁸. However, there has been no direct investigation into the electronic structure of 1T-PdSeTe so far.

Here, we examine the structural, electronic, and superconducting properties of 1T-PdSeTe single crystal. We have revealed that the superconducting transition temperature enhances up to $T_C = 3.2$ K, which is almost twice as high as $T_C = 1.6$ K in 1T-PdTe₂. By scanning transmission electron microscopy (STEM), we have confirmed that the Se and Te atoms are homogeneously distributed in the chalcogen layers, but the lattice is compatible with the CdI₂-type, consistent with X-ray diffraction. Our supercell calculation indicated preserved band degeneracy regardless of the loss of the centrosymmetric point due to the disorders in the chalcogen layers. Based on energy-band mapping in three-dimensional momentum space by angle-resolved photoemission spectroscopy (ARPES) using tunable synchrotron radiation, we confirmed the existence of TSSs and the overall band dispersions are similar to those in 1T-PdTe₂¹¹. Based on the local symmetry confirmed by STEM and energy-band dispersions observed by ARPES, the Se substitution can be regarded as applying a uniform chemical pressure which is likely related to the T_C enhancement. Our results provide insight into the effects of solid solution on the surface and bulk electronic states as well as the superconducting transition temperature.

II. EXPERIMENTAL

High-quality PdSeTe single crystals were synthesized by a two-step melting method. A stoichiometric amount of high-purity Pd wire (99.999%), Se shots (99.999%), and Te shots (99.999%) were loaded inside a double

quartz ampoule and sealed at a pressure of 4×10^{-5} torr. The sealed quartz ampoule was slowly (50 °C/hr) heated to 700 °C, kept there for 72 hrs, and cooled to room temperature at 25 °C/hr. This process was repeated three times with grounding the sample after each heat treatment to ensure homogeneous mixing. In the final step, the sample was pressed into pellets and sealed in a double quartz ampule at a pressure of 2×10^{-5} Torr. The ampule was slowly heated up to 950 °C and kept there for 24 hrs, then slowly cooled to 550 °C at 3 °C/hr, annealed for 72 hrs at 550 °C, and then cooled to room temperature at 30 °C/hr.

Powder and single crystal X-ray diffraction (XRD) measurements were performed on the as-grown PdSeTe sample using a Rigaku SmartLab X-ray diffractometer with Cu K α radiation ($\lambda=1.54 \mbox{\normalfont\AA}$). Powder X-ray diffraction (XRD) was carried out on both as-grown PdSeTe single crystal and powdered samples. The lattice parameters were evaluated by the Rietveld refinement of the XRD patterns using FullProf software. Laue diffraction measurements further confirmed the quality of the PdSeTe single crystal.

The elemental composition of freshly cleaved samples was studied using an electron probe micro-analyzer (EPMA) (Model no: JEOL JXA-iSP100).

The temperature-dependent resistivity measurement was carried out using a Physical Property Measurement System (PPMS, Quantum Design Inc., USA) in the temperature range of $0.5-300~\mathrm{K}$ with the standard four-probe contact configuration.

Transmission electron microscopy (TEM) and scanning TEM (STEM) measurements were done by Eurofins, EAG Laboratories. The STEM lamella with the face of (100) of PdSeTe was prepared using a focused ion beam on an FEI Helios Dual Beam system and was subsequently thinned to ~ 50 nm to achieve electron transparency. Imaging of the sample was performed using an FEI Titan S/TEM system operating at an accelerating voltage of 200 kV with ~ 1 Å resolution. Two STEM imaging modes were employed: annular darkfield STEM (ADF STEM) and bright-field STEM (BF-STEM). These modes provided complementary information on the sample's structure and composition. Additionally, energy-dispersive X-ray spectroscopy (EDS) data were acquired using Velox software, offering elemental composition information correlated with the highresolution imaging data.

The ARPES measurement using synchrotron radiation (SR) was carried out at BL-1 at the Research Institute for Synchrotron Radiation Science (HiSOR), Hiroshima University^{25,26} and BL5U of UVSOR-III Synchrotron, Institute for Molecular Science²⁷. The energy and angular resolutions were set at ~ 20 meV and 0.1° , respectively. The samples were cleaved in situ at ~ 20 K using the ceramic top-post method at a base pressure better than 3.0×10^{-9} Pa. We estimated k_z assuming the nearly free-electron final-state approximation with an inner po-

tential of $V_0 = 10 \text{ eV}$:

$$k_z = \sqrt{\frac{2m}{\hbar^2} \left(E_k \cos^2 \theta + V_0 \right)}$$

where E_k is the kinetic energy of the emitted photoelectrons.

III. RESULTS

A. XRD and EPMA

Fig. 1 (a) and (b) respectively show the powder XRD and single crystal XRD results. The inset of Fig. 1 (a) shows Laue diffraction patterns obtained from a (001) cleaving plane (c-plane) exhibiting hexagonal symmetry. In the previous studies, the CdI₂-type crystal structure, namely the space group of P $\bar{3}$ m1 (No. 164), was assumed to analyze the XRD data^{24,28}. If one of the Te layers in the unit cell is completely replaced by a Se layer, the inversion symmetry point will be lost, and the crystal structure should be the space group P3m1 (No. 156), as shown in Fig. 1 (c). The refined χ^2 values for P $\bar{3}$ m1 and P3m1 are, however, almost comparable, and we could not distinguish these two space groups. Below, we will discuss the crystal structure based on our STEM measurements.

The obtained lattice parameters were a = b = 3.901 Åand c = 4.978 Å, and the cell volume was 65.605 Å³. The calculated α , β , and γ angles were 90°, 90°, and 120°, which were consistent with previous studies^{8,29}. As the atomic radius of Se is smaller than that of Te, the lattice parameters a and c of PdSeTe are smaller than those of 1T-PdTe₂ by 3.49% and 3.47%, respectively. However, the value of $c/a \approx 1.27$ was the same for PdSeTe and 1T-PdTe₂. Since the c/a ratio is less than the ideal hcp lattice value $\sqrt{8/3} \approx 1.63^{30,31}$, the local O_h symmetry centered at the Pd site is lowered to the D_{3d} symmetry. Due to the enhanced overlap integral along the c-axis ($\langle 100 \rangle$ direction), the bonding and antibonding energy splitting is assumed to be larger along the c-axis direction. Due to the decrease of lattice parameters, the overall unit cell volume of PdSeTe is reduced by 10% compared with that of 1T-PdTe₂.

The EPMA measurements were done on three single crystal samples (cut from different positions of the ingot) and we obtained compositions from thirteen different positions on each sample. On average, we obtained Pd \approx 33.56%, Se \approx 31.48%, and Te \approx 34.96%, and then the composition of the sample can be written as $PdSe_{1-\delta}Te_{1+\delta}$ ($\delta\approx0.05$).

B. TEM/STEM

To visualize the real space crystal structure and identify atom species, we have measured STEM imaging

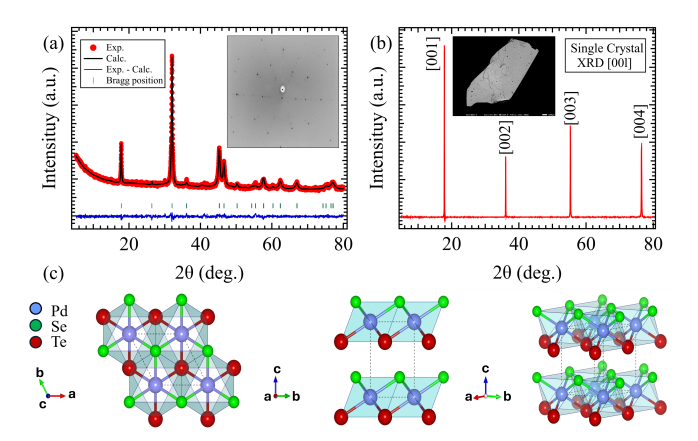


FIG. 1. (a) Rietveld refinement profile of the XRD data for PdSeTe powder sample. The red dots represent the measured data, and the solid black line represents the calculated profile. The vertical bars in green show Bragg's reflections for the CdI₂-type structure. The blue curve shows the difference between measured data and the calculated profile. Inset of (a) shows Laue's diffraction pattern of PdSeTe on the cleaved surface. (b) Single crystal XRD data for the PdSeTe sample. The inset of (b) shows the scanning electron microscope image of the sample used for EPMA analysis. (c) Crystal structure of PdSeTe compatible with the space group P3m1 (No. 156) plotted by the VESTA software.

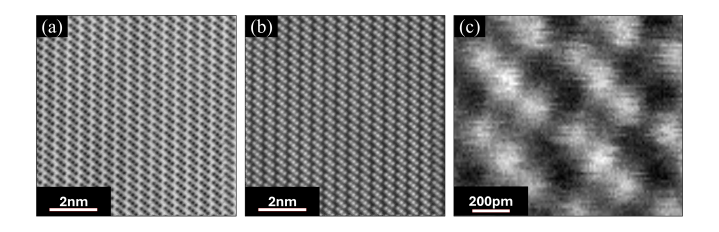


FIG. 2. High-resolution STEM image of the (100) plane of a 1T-PdSeTe crystal. (a) and (b) show the bright-field image and high-angle annular dark-field (HAADF) image, respectively. (c) Magnified atomic resolution HAADF image.

with atomic resolution for the (100) plane of PdSeTe. Fig. 2 shows a high-angle annular dark-field scanning transmission electron microscopy (HAADF-STEM) image of PdSeTe for the (100) cross-section. Here, the incident electron beam is parallel to the a-axis, namely, $\langle 100 \rangle$ direction. As the sample thickness is ~ 50 nm $\approx 123a$, the electron transmission intensity is averaged over ≈ 123 atoms along the $\langle 100 \rangle$ direction. Within about 10×10 nm² area, we observed a highly homogeneous lattice image consistent with the CdI₂ structure. Based on the length of 15–22 unit cells in the TEM image in Fig. 2 (b), we have estimated a=4.05 Å⁻¹ and c=5.12 Å⁻¹, which were only 3–4% larger than the XRD data. It was more than expected given the instrumental resolution of ~ 1 Å.

In Figs. 3(a)–3(c), the energy-dispersive X-ray spectroscopy (EDX) maps show the elemental distribution of

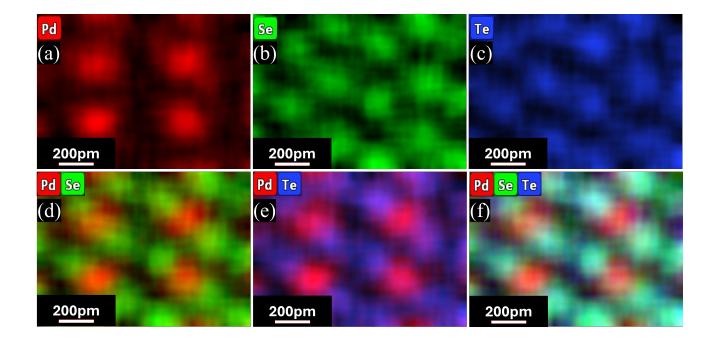


FIG. 3. Atomically resolved HAADF-STEM EDX mappings of PdSeTe single crystal. (a), (b), and (c) show signals from Pd (red), Se (green), and Te (blue) atoms, respectively. (d) shows the overlaid image of (a) and (b). (e) shows the overlaid image of (a) and (c). (f) shows the overlaid image of (a), (b), and (c).

Pd (red), Se (green), and Te (blue) obtained by STEM. The Pd and Se contributions are overlaid in Fig. 3(d) and Pd and Te contributions are overlaid in Fig. 3(e). It is clearly seen that Pd atoms are well separated from the Se and Te atoms, indicating that Pd layers are occupied by Pd atoms only. On the other hand, Figs. 3(b) and 3(c) indicate Se and Te atoms almost overlap, suggesting these atoms equally occupy the chalcogen layers. In Fig. 3(f), Pd, Se, and Te contributions are all overlaid, and one can confirm Se and Te atoms are mixed in the chalcogen layers. To further confirm the results, we checked the intensity distribution of the HAADF-STEM image which is sensitive to atomic number (Z). As Te is heavier than Se, the intensity should be stronger. However, the intensity of chalcogen layers is highly homogeneous indicating that Se and Te atoms are evenly mixed in the chalcogen layers.

C. Resistivity and Magnetic Susceptibility

Figure 4(a) shows the temperature dependence of the electrical resistivity (ρ) from 0.5 K to 300 K. In Fig. 4(b), the resistivity abruptly drops to zero at the superconducting transition temperature (T_C) of 3.2 K. The observed T_C is almost twice as high as that of PdTe₂ (1.64 K) and even larger than the value, 2.74 K, previously reported for PdSeTe⁸.

Figs. 5(a) and 5(b) show temperature-dependent magnetic susceptibility measured in zero-field-cooled (ZFC) and field-cooled (FC) modes under an external magnetic field (H) of 15 Oe parallel to the c-axis and perpendicular to the c-axis, respectively. One can see a superconducting transition at 3.2 K in both modes, in agreement with the resistivity data. The superconducting volume fraction was estimated to be 95.5% for $H \parallel c$ [Fig. 5(a)] and 90.0% for $H \perp c$ [Fig. 5(b)]. These results suggest possible existence of surface superconductivity contribution of $\sim 5\%$, though most of the contribution is from the bulk.

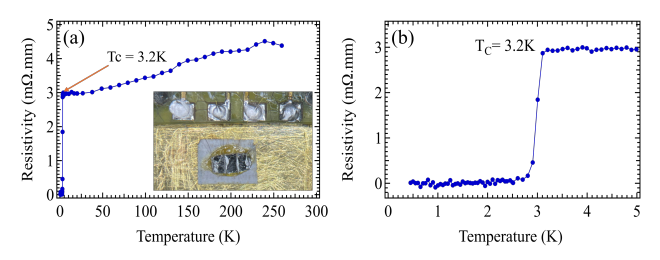


FIG. 4. (a) Resistivity as a function of temperature (Inset: four probe connections on PPMS sample stage). (b) Enlarged view of resistivity near the superconducting transition temperature.

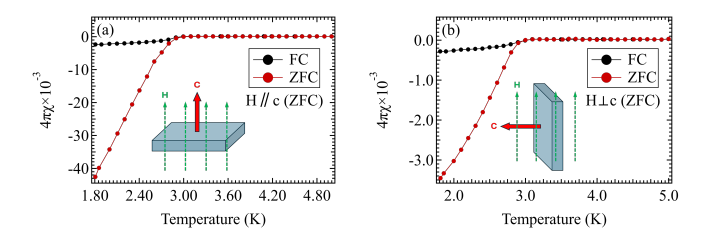


FIG. 5. Temperature dependence of magnetic susceptibility measured in FC and ZFC mode with an external field of 1.5 mT. (a) Magnetic field is parallel to the c-axis $(H \parallel c)$. (b) Magnetic field is perpendicular to the c axis $(H \perp c)$.

D. Electronic structure calculation

To understand the electronic structure of PdSeTe, we have performed density functional theory (DFT) calculations. We used the FLEUR DFT package³², which utilizes a full-potential linearized augmented plane-wave and local orbitals (FP-LAPW+lo) basis³³⁻³⁵ along with the Perdew-Burke-Ernzerhof parametrization of the generalized gradient approximation as the exchangecorrelation functional³⁵. The plane-wave cutoff parameter was set to five times the largest muffin-tin radius, and the irreducible Brillouin zone was sampled by a $10 \times 10 \times 12$ mesh of k-points for the bulk calculations and an $18 \times 18 \times 1$ mesh of k-points for the slab model calculations. The lattice parameters used in the calculations were taken from experimental measurements. Spinorbit coupling was included as a second variational procedure. Irreducible representations were determined using the built-in irrep tool in $FLEUR^{32}$.

Fig. 6(a) and Fig. 6(b) respectively show the DFT calculation results of the bulk bands of 1T-PdTe_2 with the space group of $P\bar{3}\text{m1}$ (No. 164) and those of PdSeTe with the space group of P3m1 (No. 156). Due to the loss of the centrosymmetric point in PdSeTe, the degeneracy of the Kramers doublet protected by the inversion symmetry are lifted along most of the high symmetry directions except for the Γ -A direction. We should note that along the Γ -A direction, the basis function is 1 or z and the C_{3v} symmetry properties are not affected by the loss of the inversion symmetry point.

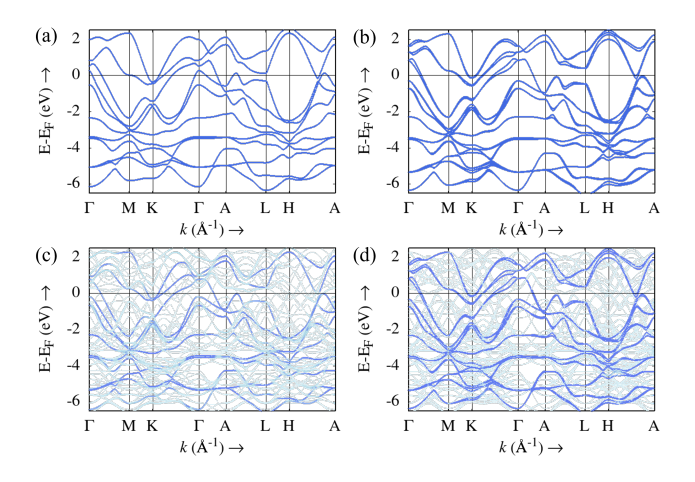


FIG. 6. (a) The bulk DFT calculations of PdTe₂ with the space group of P $\bar{3}$ m1 (No. 164). (b) The bulk DFT calculations of PdSeTe with the space group of P3m1 (No. 156). (c) The DFT calculations of the bulk bands on $2\times2\times2$ supercell of PdSeTe where an even number of the Se and Te atoms occupy the chalcogen layer, breaking the space group symmetry of P3m1 (No. 156). (d) The DFT calculations on a $2\times2\times2$ supercell but with the well-defined Se and Te layers to hold the space group symmetry of P3m1 (No. 156). The energy bands in (c) and (d) are unfolded into the Brillouin zone of the CdI₂ type crystal structure. The unfolded energy bands in (d) are consistent with those of (b).

To understand the disorder effect in the chalcogen layers as revealed by STEM measurements, we have calculated the band structure for a $2 \times 2 \times 2$ supercell where an even number of Se and Te atoms occupy the chalcogen layer, breaking the space group symmetry of P3m1 (No. 156). To further confirm the symmetry breaking effect, we also performed the DFT calculations on a $2 \times 2 \times 2$ supercell assuming the space group P3m1 (No. 156) where one of the chalcogen layers in the unit cell is completely replaced by Se atoms as shown in Fig. 6(d). The energy bands in Figs. 6(c) and 6(d) are unfolded into the Brillouin zone of the CdI₂-type crystal structure.

One can confirm that the band dispersions shown in Fig. 6(b) and 6(d) are identical for PdSeTe with the space group of P3m1 (No. 156). On the other hand, in Fig. 6(c), the supercell calculation with disordered chalcogen layers does not show splitting as shown in Figs. 6(b) and 6(d), which is similar to PdTe₂ in Fig. 6(a). It suggests that when Se and Te atoms are randomly arranged in the chalcogen layer, 50% each, the inversion symmetry appears to be restored effectively. One can clearly see the type-II Dirac points along the Γ -A direction in Fig. 6(c). By detailed comparison between Fig. 6(a) [PdTe₂] and 6(c) [disordered PdSeTe], in disordered PdSeTe, one of the hole-like bands at the Γ point is completely occupied and the saddle point just above the $E_{\rm F}$ at the M point is elevated. Along the A-H and A-L lines, small hole-like and electron-like bands do not cross the $E_{\rm F}$ in disordered PdSeTe.

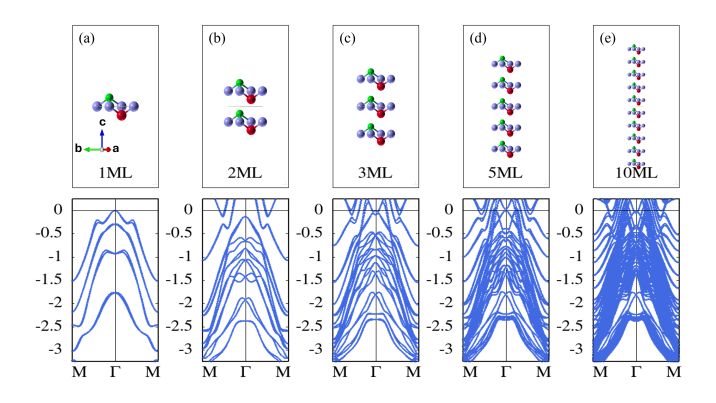


FIG. 7. Thickness-dependent DFT calculations (a) 1ML, (b) 2ML, (c) 3ML, (d) 5ML and (e) 10ML.

To understand the surface-derived states, we have done DFT calculations on slab models for different monolayer (ML). Here we did not consider the disorder effect in the chalcogen layers. We assume the disorder effect does not significantly alter the band positions based on the results of supercell calculations in Figs. 6(c) and 6(d). As shown below the results gave reasonable explanations for the ARPES results. The slab was constructed by stacking five unit-cells along the c-direction with a 4.978 Å vacuum gap.

Figs. 7(a)-7(e) show the calculated results from 1ML up to 10ML. At the $\bar{\Gamma}$ point and at the energy of -1.5 eV and -1.8 eV, one can clearly see Dirac-fermion-like crossings which should correspond to the topological surface states (TSS1 and TSS2 reported in $PdTe_2^{14}$). The former TSS falls in the bulk band projection but the latter TSS resides within the gap of the bulk band projection. Due to the parity inversion in the bulk bands, these two states are topologically non-trivial¹⁴. In our calculation, the Dirac point at -1.8 eV is robust even in 1ML while recent thickness-dependent DFT calculations on $PdTe_2$ indicated gap opening at the Dirac point below $3ML^9$. Note that the electron-like topologically nontrivial surface states exist near the E_F around the middle points of the $\bar{\Gamma}$ - \bar{M} line.

E. Angle-resolved photoemission spectroscopy

Fig. 8(a) shows the Fermi surface cross section by the plane k_x-k_z taken with various photon energies ranging from 25 eV up to 100 eV. Here k_x and k_z directions are parallel to $\bar{\Gamma}$ - $\bar{\rm M}$ direction and Γ -A direction, respectively. One can see k_z -independent features around $k_x=\pm 0.5$ Å⁻¹, which correspond to the topological surface states at the $E_{\rm F}$. Fig. 8(b) shows the ARPES intensity map exhibiting the band structure along the $\bar{\Gamma}$ - $\bar{\rm M}$ direction. The topological surface state near the $E_{\rm F}$ exists around $k_x=\pm 0.5$ Å⁻¹, which is consistent with our 5ML slab calculation in Fig. 8(c). Furthermore, one can see a Dirac cone-like topological surface state located -1.75

eV below the $E_{\rm F}$ at the $\bar{\Gamma}$ point. The overall spectral features are similar to the ARPES results shown in PdTe₂ especially closer to the A point $(h\nu \sim 60 \text{ eV})^{9-11}$.

As shown below, there exist k_z -dependent features which allow us to determine the inner potential, and $h\nu=26$ eV ARPES result is actually close to the A point of the bulk Brillouin zone. Fig. 8(d) shows the theoretical dispersion along the L-A-L high symmetry line for a supercell with disordered Se and Te atoms in the chalcogen layer. The electron-like band near the $E_{\rm F}$ centered at the A point in Fig. 8(d) reproduces the observed electron-like band at the $\bar{\Gamma}$ point in Fig. 8(b). The flat band at the $\bar{\Gamma}$ point at -2.5 eV in Fig. 8(d) also exhibits corresponding spectral features around -2.5 eV, but the dispersion is somewhat larger around the A point.

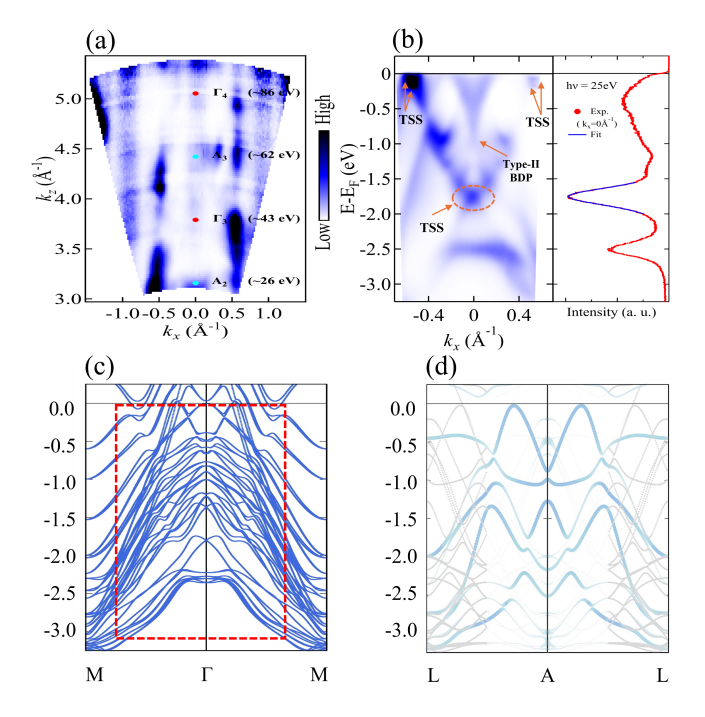


FIG. 8. (a) Fermi surface cross section of PdSeTe by the k_x-k_z plane. Here k_x and k_z directions are parallel to $\bar{\Gamma}-\bar{M}$ direction and $\Gamma-A$ direction, respectively. To scan the k_z direction we changed photon energy from 26 eV up to 100 eV. (b) ARPES intensity plot taken at $h\nu=25$ eV near the A point. The orange dashed ellipse shows the Dirac-cone-like topological surface state. (c) The DFT calculation result for 5 ML along the $\bar{M}-\bar{\Gamma}-\bar{M}$ high-symmetry direction. The red box corresponds to the range of the ARPES image in (b). (d) The DFT calculation result of the bulk band dispersions along L-A-L direction obtained from a supercell with disordered Se and Te atoms.

Figs. 9(a)–9(j) show constant energy contours from the $E_{\rm F}$ down to -2.25 eV. Here k_x and k_y directions are parallel to $\bar{\Gamma}$ – $\bar{\rm M}$ direction and $\bar{\Gamma}$ – $\bar{\rm K}$ direction, respectively. While the Fermi surface intensity distribution in Fig. 9(a) shows nearly six-fold symmetric, there exists three-fold symmetric intensity modulation for lower en-

ergies, which is likely due to the matrix element effect.

Here, the $\bar{\Gamma}$ point of the surface Brillouin zone is close to the A point of the bulk Brillouin zone. The circular Fermi surface around the $\bar{\Gamma}$ point matches the bulk derived electron-like band as shown in Fig. 8(d). With lowering energy, this Fermi surface shrinks to a point at an energy of -0.75 eV, where the bottom of the electron-like energy band is located as shown in Fig. 8(b). On the other hand, in Fig. 9(h), one can see the Dirac point of the topological surface state at the $\bar{\Gamma}$ point at the energy of -1.75 eV as shown in Fig. 8(b).

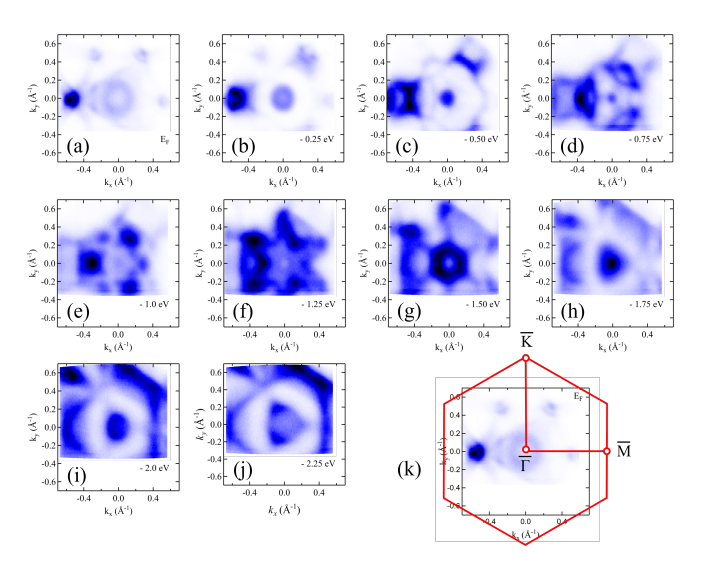


FIG. 9. (a)–(j) Constant energy contour from the $E_{\rm F}$ down to -2.25 eV. Here k_x and k_y directions are parallel to $\bar{\Gamma}$ – $\bar{\rm M}$ direction and $\bar{\Gamma}$ – $\bar{\rm K}$ direction, respectively. The bottom of the electron-like band centered at the $\bar{\Gamma}$ point exists at the energy of -0.75 eV. The Dirac point of the topological surface state exists at the $\bar{\Gamma}$ at the energy of -1.75 eV. (k) The first Brilluoin zone overlaid on (a).

To obtain further evidence of the bulk-derived band, we show band dispersion along k_z direction at $k_x = -0.40$ Å⁻¹ in Fig. 10(a) and at $k_x = 0.40$ Å⁻¹ in Fig. 10(b). While the intensity is much stronger in Fig. 10(a) than that in Fig. 10(b) which is likely due to the matrix element effect, we assume the dispersive features existing between -1.0 eV and -2.0 eV should be the same. We also detect k_z -independent dispersion at -1.0 eV around $k_z = 2.8$ Å⁻¹, exhibiting a band crossing similar to the tilted Dirac point.

To investigate details of the band crossing, we examined the k_x-k_z map at the energy of -1.3 eV [Fig. 11(a)], -0.93 eV [Fig. 11(b)], and -0.6 eV [Fig. 11(c)]. There are two k_z -independent lines at $k_x \sim \pm 0.40$ Å⁻¹, which is derived from the TSS above the Dirac point at -1.75 eV. In addition, one can see a dispersive feature at $k_x \sim \pm 0.5$ Å⁻¹ and $k_z \sim 3.0$ Å⁻¹ in Fig. 11(a) and $k_x \sim 0$ Å⁻¹ and $k_z \sim 2.8$ Å⁻¹ in Fig. 11(b). These results indicate the surface and bulk derived states cross around -1.0 eV around $k_z = 2.8$ Å⁻¹, and form a type-II

Dirac point.

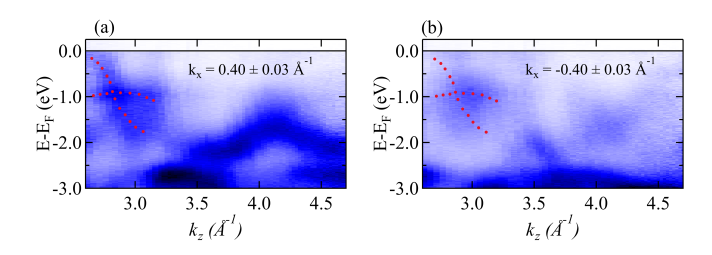


FIG. 10. Band dispersion along A–Γ–A direction (a) $k_x = 0.40 \pm 0.02 \text{ Å}^{-1}$, (b) $k_x = -0.40 \pm 0.02 \text{ Å}^{-1}$.

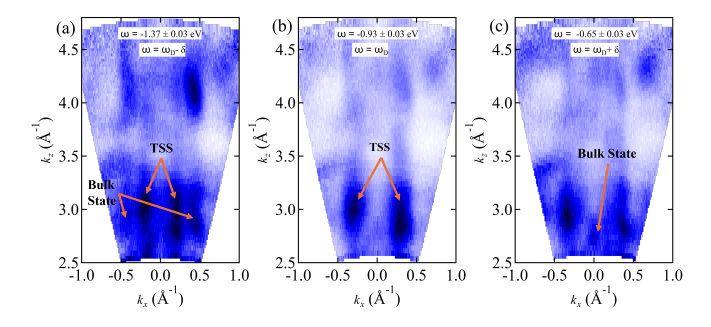


FIG. 11. $k_x - k_z$ dispersion along Γ -A direction (a) band dispersion below the Dirac point energy (b) at the Dirac point energy (c) above the Dirac point energy.

IV. DISCUSSION

In this study, the TEM/STEM image exhibited the local lattice structure compatible with the CdI₂-type with homogeneously mixed Se and Te atoms in the chalcogen layers, which is consistent with the XRD analyses. In addition, we have revealed that the bulk and surface-derived energy-band structures in the momentum space are similar to 1T-PdTe₂, regardless of the disorder in Se and Te atoms in the chalcogen layers. These results may allow us to discuss the increase of the superconducting transition temperature from the viewpoint of the chemical pressure effect.

C. Soulard et al. examined the lattice parameter and unit cell volume of 1T-PdTe_2 as a function of external pressure³⁶. They found that above 15 GPa the intralayer Te-Te distance abruptly expanded and the interlayer Te-Te distance reduced at room temperature³⁶. However, the unit cell volume as a function of pressure showed continuous temperature dependence without anomaly. Based on the reduction of the unit cell volume by 10% for PdSeTe, the chemical pressure is equivalent to an external pressure of 9 GPa³⁶. On the other hand, H. Leng et al. reported that while T_C enhanced from 1.6 K at ambient pressure up to 1.9 K at 1.0 GPa, T_C reduces above the 1.0 GPa³⁷. It indicates external pressure cannot increase T_C more than 2 K, exhibiting sharp

contrast to the chemical pressure induced by solid solution. Meanwhile, W. Liu et al. studied T_C of solid solution $PdSe_{2-x}Te_x$ for $x = 1.0, 1.1, 1.2^{24}$. T_C tends to increase with increasing Se concentration (i.e., chemical pressure) 24 keeping CdI₂-type crystal structure, *i.e.*, P3m1 (No. 164)²⁴. They argued the disorder/defect effects in the enhancement of T_C in addition to the chemical pressure²⁴. While we observed homogeneously mixed Se and Te atoms in the chalcogen layers, the lattice structure as detected by TEM/STEM is rather well defined to be CdI₂ type crystal structure. Furthermore, although the ARPES linewidth is somewhat broader due to the disorder/defects scattering, the band dispersion and topological property are still well identified. While we need further study to quantitatively explain the enhancement of T_C based on fine details of the Eliashberg function, present results provide the fundamental ground to understand the topological and superconducting properties of solid solution of PdSeTe.

V. CONCLUSION

We have grown single crystals of 1T-PdSeTe and investigated their crystal structure, electronic structure, and superconducting properties. The resistivity measurements indicated the superconducting transition temperature (T_C) of 3.2 K, which was approximately twice as high as that of 1T-PdTe₂ ($T_C = 1.64$ K). Our magnetic susceptibility measurements revealed a small fraction of surface superconductivity. The scanning transmission electron microscopy showed that Se and Te atoms were homogeneously mixed in the chalcogen layers and that the local symmetry was consistent with the CdI₂-type crystal structure. Angle-resolved photoemission spectroscopy results and density functional theory calculations indicated the presence of topological surface states (TSSs) and overall similarity to the bulk-band dispersion of 1T-PdTe₂. These results suggest that the TSSs remain robust despite atomic disorder in the chalcogen layers. As the electronic band dispersion and local structures are well-characterized, the enhancement in T_C is likely associated with the chemical pressure. Our findings provide insight into how solid solution influences on surface and bulk electronic states, as well as the superconducting transition temperature.

VI. ACKNOWLEDGMENTS

YK acknowledges Hiroshima University for providing the Graduate School Research Fellowship. YK also thanks Prof. Akio Kimura, Prof. Taichi Okuda, and Prof. Takeshi Matsumura for their valuable discussions and suggestions. YK and KS acknowledge the experimental facilities (XRD and EPMA) at N-BARD, Hiroshima University. The ARPES measurements were performed with the approval of the Proposal Assessing

Committee of the Hiroshima Synchrotron Radiation Center (Proposal Number: 22AU002). We thank N-BARD,

Hiroshima University, for supplying the liquid helium. This work is partially supported by Grants-in-Aid for Scientific Research (22K03495).

- * d225570@hiroshima-u.ac.jp
- † shivam.physics@gmail.com
- [‡] kshimada@hiroshima-u.ac.jp
- ¹ M. Z. Hasan and C. L. Kane, Rev. Mod. Phys. **82**, 3045 (2010).
- ² M. Neupane, S.-Y. Xu, R. Sankar, N. Alidoust, G. Bian, C. Liu, I. Belopolski, T.-R. Chang, H.-T. Jeng, H. Lin, et al., Nature communications 5, 3786 (2014).
- ³ B. Yan and C. Felser, Annual Review of Condensed Matter Physics 8, 337 (2017).
- ⁴ B. Lv, T. Qian, and H. Ding, Reviews of Modern Physics 93, 025002 (2021).
- ⁵ X. Wan, A. M. Turner, A. Vishwanath, and S. Y. Savrasov, Physical Review B—Condensed Matter and Materials Physics 83, 205101 (2011).
- ⁶ H. B. Nielsen and M. Ninomiya, Physics Letters B 130, 389 (1983).
- ⁷ T. Nag and S. Nandy, Journal of Physics: Condensed Matter 33, 075504 (2020).
- ⁸ W. Liu, S. Li, H. Wu, N. Dhale, P. Koirala, and B. Lv, Physical Review Materials 5, 014802 (2021).
- ⁹ J. Cook, S. Mardanya, Q. Lu, C. Conner, M. Snyder, X. Zhang, J. McMillen, G. Watson, T.-R. Chang, and G. Bian, Nano letters 23, 1752 (2023).
- O. Clark, M. Neat, K. Okawa, L. Bawden, I. Marković, F. Mazzola, J. Feng, V. Sunko, J. Riley, W. Meevasana, et al., Physical review letters 120, 156401 (2018).
- ¹¹ M. Bahramy, O. Clark, B.-J. Yang, J. Feng, L. Bawden, J. Riley, I. Marković, F. Mazzola, V. Sunko, D. Biswas, et al., Nature materials 17, 21 (2018).
- ¹² B. A. Bernevig, T. L. Hughes, and S.-C. Zhang, science 314, 1757 (2006).
- ¹³ R. Yu, W. Zhang, H.-J. Zhang, S.-C. Zhang, X. Dai, and Z. Fang, science **329**, 61 (2010).
- ¹⁴ L. Fu and E. Berg, Physical review letters **105**, 097001 (2010).
- ¹⁵ X.-L. Qi, R. Li, J. Zang, and S.-C. Zhang, science **323**, 1184 (2009).
- ¹⁶ K. Kim, S. Kim, J. Kim, H. Kim, J.-H. Park, and B. Min, Physical Review B 97, 165102 (2018).
- ¹⁷ G. Anemone, P. Casado Aguilar, M. Garnica, F. Calleja, A. Al Taleb, C.-N. Kuo, C. S. Lue, A. Politano, A. L. Vázquez de Parga, G. Benedek, et al., npj 2D Materials and Applications 5, 25 (2021).
- P. P. Ferreira, A. L. Manesco, T. T. Dorini, L. E. Correa, G. Weber, A. J. Machado, and L. T. Eleno, Physical Review B 103, 125134 (2021).
- W. Xia, J. Wu, C. Xia, Z. Li, J. Yuan, C. An, X. Liu, X. Wang, N. Yu, Z. Zou, et al., Small, 2402749 (2024).

- ²⁰ C. Liu, C.-S. Lian, M.-H. Liao, Y. Wang, Y. Zhong, C. Ding, W. Li, C.-L. Song, K. He, X.-C. Ma, W. Duan, D. Zhang, Y. Xu, L. Wang, and Q.-K. Xue, Phys. Rev. Mater. 2, 094001 (2018).
- ²¹ F. Fei, X. Bo, R. Wang, B. Wu, J. Jiang, D. Fu, M. Gao, H. Zheng, Y. Chen, X. Wang, H. Bu, F. Song, X. Wan, B. Wang, and W. Guanghou, Physical Review B 96, 041201 (2017).
- ²² S. Das, A., A. Sirohi, L. Yadav, S. Gayen, Y. Singh, and G. Sheet, Physical Review B **97**, 014523 (2018).
- ²³ R. Xiao, C. Cheung, P. Gong, W. Lu, J. Si, and Y. Sun, Journal of Physics: Condensed Matter 30, 245502 (2018).
- W. Liu, M. R. Osanloo, X. Wang, S. Li, N. Dhale, H. Wu, M. L. Van de Put, S. Tiwari, W. G. Vandenberghe, and B. Lv, Physical Review B 104, 024507 (2021).
- ²⁵ K. Shimada, M. Arita, T. Matsui, K. Goto, S. Qiao, K. Yoshida, M. Taniguchi, H. Namatame, T. Sekitani, K. Tanaka, et al., Nuclear Instruments and Methods in Physics Research Section A: Accelerators, Spectrometers, Detectors and Associated Equipment 467, 504 (2001).
- ²⁶ H. Iwasawa, K. Shimada, E. Schwier, M. Zheng, Y. Ko-jima, H. Hayashi, J. Jiang, M. Higashiguchi, Y. Aiura, H. Namatame, et al., Journal of Synchrotron Radiation 24, 836 (2017).
- ²⁷ H. Ota, E. Salehi, M. Fujimoto, K. Hayashi, T. Horigome, H. Iwayama, M. Katoh, N. Kondo, S. Makita, F. Matsui, et al., Journal of Physics: Conference Series 2380, 012003 (2022).
- E. McCarron, R. Korenstein, and A. Wold, Materials Research Bulletin 11, 1457 (1976).
- ²⁹ F. Hulliger, Journal of Physics and Chemistry of Solids 26, 639 (1965).
- ³⁰ T. Finlayson, W. Reichardt, and H. Smith, Physical Review B 33, 2473 (1986).
- ³¹ H.-J. Noh, J. Jeong, E.-J. Cho, K. Kim, B. Min, and B.-G. Park, Physical review letters **119**, 016401 (2017).
- ³² D. Wortmann, G. Michalicek, N. Baadji, M. Betzinger, G. Bihlmayer, J. Bröder, T. Burnus, J. Enkovaara, F. Freimuth, C. Friedrich, et al., Zenodo 10.5281/zenodo.7576163 (2023).
- ³³ D. Singh, Phys. Rev. B 43, 6388 (1991).
- ³⁴ E. Wimmer, H. Krakauer, M. Weinert, and A. J. Freeman, Physical Review B 24, 864 (1981).
- M. Betzinger, C. Friedrich, and S. Blügel, Physical Review B—Condensed Matter and Materials Physics 81, 195117 (2010).
- ³⁶ C. Soulard, P. Petit, P. Deniard, M. Evain, S. Jobic, M.-H. Whangbo, and A.-C. Dhaussy, Journal of Solid State Chemistry 178, 2008 (2005).
- ³⁷ H. Leng, A. Ohmura, L. N. Anh, F. Ishikawa, T. Naka, Y.-K. Huang, and A. de Visser, Journal of Physics: Condensed Matter 32, 025603 (2019).